



Buckypaper embedded self-sensing composite for real-time fatigue damage diagnosis and prognosis

Siddhant Datta^{*}, Rajesh Kumar Neerukatti, Aditi Chattopadhyay

School for Engineering of Matter, Transport and Energy, Arizona State University, Tempe, AZ, 85281, USA

ARTICLE INFO

Article history:

Received 18 January 2018

Accepted 25 June 2018

Available online 29 June 2018

Keywords:

Carbon nanotubes

Buckypaper

Fatigue

Glass fiber

Self-sensing

Prognosis

ABSTRACT

In this study, buckypaper (BP) membranes have been used to introduce self-sensing capability in glass fiber reinforced polymer matrix (GFRP) laminates by embedding them in the interlaminar region of the laminates. Piezoresistive characterization studies were conducted by subjecting the self-sensing GFRP (SGFRP) specimens to cyclic loading and high sensitivity to strain was observed. A measurement model for real-time quantification of fatigue crack, developed using *in-situ* resistance measurements obtained under fatigue loading, was used to quantify fatigue crack length in real time. The fatigue crack growth rates and the nature of crack propagation in baseline and SGFRP specimens were compared. The results show that the introduction of BP reduced the average crack growth rate by an order of magnitude as a result of crack tip blunting during fatigue, while facilitating real time strain sensing and damage quantification. A fully probabilistic prognosis methodology was also developed by combining the *in-situ* measurement model with a machine learning based prognosis model to accurately predict the real-time fatigue crack propagation using sequential Bayesian techniques.

© 2018 Elsevier Ltd. All rights reserved.

1. Introduction

Fiber reinforced polymer (FRP) composites are extensively used in aerospace and automotive industry mainly due to their high specific strength, reasonable fatigue life and low cost. However, monitoring damage in composites using real-time sensors or non-destructive evaluation techniques is a challenging task due to their complex and heterogeneous microstructure. Recently, the aerospace industry has focused its research on developing multifunctional composites with superior mechanical properties and self-sensing capabilities that enable the composite to autonomously sense deformation and damage in real-time. Self-sensing capability is an important feature that can reduce maintenance and inspection time while increasing the safety of aerospace structures [1,2]. Many recent studies have focused on employing piezoresistive property of constituent materials for structural health monitoring (SHM) of composite structures. The advantage of piezoresistive based sensing is that it does not require expensive equipment for instrumentation or the placement of discrete sensors that can compromise structural strength or performance. Of late, carbon

nanotubes (CNTs) have gained immense popularity as a multifunctional nanofiller for FRPs. The CNTs when added to FRPs form a conductive percolation network, thereby rendering the structure conductive. Owing to the conductive and piezoresistive nature of CNTs and their percolation networks, many researchers have demonstrated electrical resistance based SHM of such composite structures [3–8]. Carbon nanotubes have shown promise as nanofillers that introduce multifunctional properties in composites by considerably improving their mechanical properties such as tensile and compressive strength, elastic modulus and fatigue resistance in addition to enhancing thermal and electrical properties [9–19].

Alexopoulos et al. developed a CNT based polyvinyl alcohol fiber which, when embedded in GFRPs, enabled real time strain and damage monitoring of the GFRP under static and cyclic load [3]. Kim et al. demonstrated damage detection in 3D braided composites using dispersed CNTs in the polymer matrix and measuring the electrical resistance change of the composite as the composite was loaded [20]. Vertuccio et al. investigated the strain and damage sensing capability of CNT embedded resins under static and cyclic strain [21]. They showed that strain sensitivity of CNT based composites can be controlled by varying the weight fraction of CNT nanofiller in the host structure.

Recently, the applications of CNTs in the form of buckypaper (BP), which is a thin porous membrane of highly entangled CNTs

^{*} Corresponding author.

E-mail address: sdatta10@asu.edu (S. Datta).

held together by van der Waals forces, have received extensive recognition. Bucky paper offers versatility in a variety of applications which include water purification, gas/vapor sensing, strain sensing, fire retardant coatings, artificial muscles, EMI shielding and self-heating hybrid composites [22–26]. Rein et al. explored the effects of wide range of strains on the electrical response of BP embedded in different types of polymers [27]. They reported observing high strain-sensitivity of BP even at strains as high as 30%. The electromechanical response of the BP sensors used in their study was also found to be influenced by local defects and geometry. Zhang et al. embedded BP in glass fiber laminates for strain and damage sensing through electrical resistance measurements and analyzed BP sensitivity in different strain ranges [28]. Bucky paper was embedded in bonded joints in a study by Rai et al. and real-time strain monitoring was done using the piezoresistive response during pull off tests [29]. However, most of these studies found in literature provide a qualitative measure of damage in the material based on residual resistance increment. Also, there has been little effort done to correlate residual resistance increments to quantitatively express damage in such composites. Thus, a novel method for real time fatigue crack length quantification in a new type of BP embedded GFRP composite has been presented in this paper.

In this research, CNT BPs manufactured from a novel fabrication process have been used to successfully induce multifunctional capabilities, such as strain sensing, damage quantification and improved fatigue resistance, in GFRP laminates. The capability of this BP manufacturing process to rapidly manufacture sizable membranes is demonstrated and its potential to advance CNT membrane based composites to structural scale applications is realized through the development of self-sensing GFRPs (SGFRPs) with superior resistance to fatigue crack growth. The ability to autonomously sense and quantify strain and damage in real time has been demonstrated through *in-situ* resistance measurements during fatigue loading.

A novel damage prognosis methodology that combines highly robust machine learning based prognosis model with *in-situ* measurement models is developed [30]. The measurement model is obtained through measuring the resistance change with increase in the crack length. Since the resistance measurements can have variance in actual service life environments due to temperature variations and ambient vibrations, the measurements may not be sufficient to accurately quantify damage. Therefore, the measurement model is combined with a prognosis model capable of predicting the crack propagation accurately with in a sequential Bayesian framework [31,32]. Specifically, particle filtering was used to iteratively update the crack length predictions from the prognosis model with the resistance based crack length measurements obtained from the measurement model. The proposed methodology optimally combines the measurement model with prognosis model to accurately estimate the crack length dynamically with uncertainty quantification. This integrated approach was validated with experimental data. The methodology described above works in real-time since the resistance measurements for the measurement model are obtained real-time and the prognosis model uses the measurement information at each iteration/step.

This paper is organized as follows. In section 2, the fabrication methods followed for the BP and SGFRP are discussed along with the experimental procedures followed for their electro-mechanical characterization. The theoretical formulations for the prognosis model are presented in section 3. Section 4 presents the experimental results for piezoresistive strain sensing, fatigue crack growth behavior and real-time crack quantification in SGFRPs as well as the crack growth predictions obtained from the prognosis model.

2. Materials and methods

2.1. Fabrication of BP

The real-time self-sensing capabilities of the BP-embedded SGFRPs are demonstrated in the form of strain sensing and damage quantification under cyclic loading. Bucky papers were fabricated using multi-walled carbon nanotubes (MWNTs) that were obtained from US Research Nanomaterials Inc., with an average outer diameter of 10 nm–30 nm, average length of 15 μm –30 μm , and a purity level of 90% (as claimed by the manufacturer). A novel slurry compression process, developed in-house for high speed fabrication of sizable BPs, was used. A high concentration slurry of MWNTs and methanol was obtained by evaporating excess, free-flowing methanol from a MWNT/methanol solution using a tip-sonicator. The slurry is laid on the base compression plate as a continuous layer in the shape of a circular disc with a height of 4 mm. The top compression plate is placed in order to sandwich the slurry between the two plates and this setup is compressed using a 20-Ton hydraulic press. The surface of the compression plates are covered with plastic sheets to prevent the pressed CNT slurry from adhering to the plate surface. The setup is then dismounted from the hydraulic press and placed in an oven for drying. Next the top plate is removed and the free-standing BP is lifted off the compression plate and degassed in vacuum for 10 h. Scanning electron micrographs (SEM) of the membrane were obtained using JEOL XL-30 electron microscope to analyze the microstructure and qualitatively characterize the structural homogeneity and uniformity.

Fig. 1a shows a large size BP fabricated using this technique. The BPs used in this research had a uniform thickness of approximately 400 μm and exhibited a stable and free-standing structure. Fig. 1b shows a SEM image of the BP at low magnification (33 \times). This micrograph shows the continuous and crack-free structure of as-formed BP with absence of large voids and a fairly even surface. Fig. 1c presents a high magnification (35000 \times) SEM micrograph of the BP showing uniformly distributed, randomly oriented and highly entangled MWNT bundles. Based on these observations, it was hypothesized that the BP is homogeneous and has isotropic material properties. Details of the fabrication process and additional details on the physical structure and properties of the BP can be found in a recent publication by the authors [33].

2.2. Fabrication of self-sensing glass fiber epoxy laminates

The SGFRPs were fabricated using six layers of eight harness satin (8HS) weave of S2 glass fiber from Fibre Glax, with each layer having a thickness of approximately 0.25 mm and bulk density of 2.46 g/cc. The polymer matrix consisted of thermoset epoxy resin Epon 863 with hardener EPI-CURE 3290 (100/27 wt ratio). A wet layup procedure was followed wherein BP, spanning the gauge length of the specimen, was embedded in the center interlaminar layer (between the third and fourth glass fiber layer) of the laminate. Silver adhesive tracks were painted on to the BP surface prior to embedding to avoid the use of invasive electrodes that can often be in the form of embedded wires. Such invasive electrodes can act as hot-spots for damage initiation since they lead to local stress concentrations. The application of silver tracks directly onto the BP also results in high conductivity in the SGFRPs since the contact resistance at the electrode-BP interface is minimized. Following the wet layup procedure, the specimens were cured in a 24-ton hot-press at 150 °F for 6 h. Since the as-formed embedded BP has a porous structure, its thickness reduces to approximately 60–80 μm after the curing process is complete. Good through thickness resin penetration and impregnation is essential to enable effective load

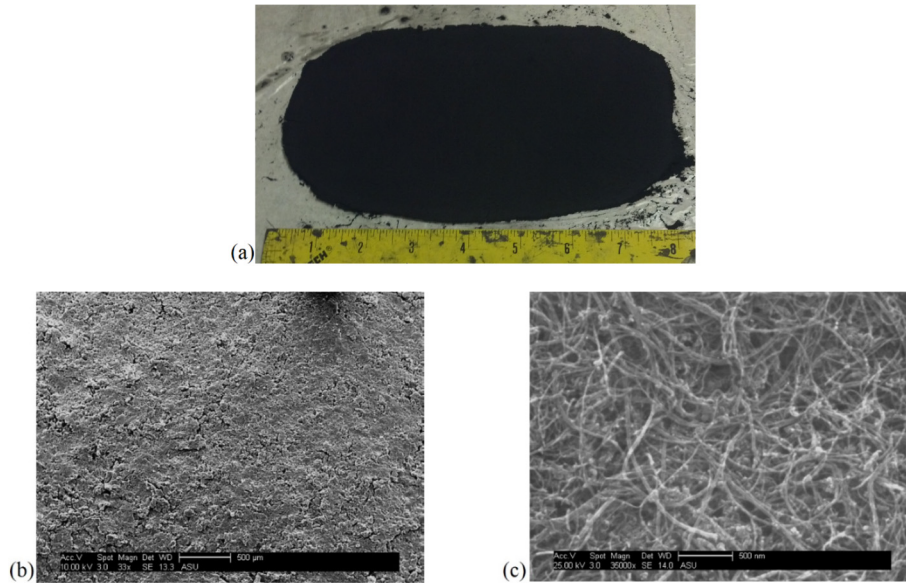


Fig. 1. (a) 20 cm × 16 cm × 400 μm BP membrane fabricated from slurry compression method; (b) SEM micrograph of BP membrane at 33× and (c) at 35000×. (A colour version of this figure can be viewed online.)

transfer to the BP and allow for efficient real-time strain sensing. The final laminate thickness after curing was approximately 1.5 mm and test specimens of size 200 mm × 25.4 mm were prepared for mechanical and piezoresistive characterization.

2.3. Strain sensing

To analyze the piezoresistive response of the SGFRP under tension-tension cyclic loading, 8" × 1" specimens without any notch were tested with a strain range of 0.002–0.009 using a MTS Bionix servo-hydraulic test system. Specimens without notch were used for the piezoresistivity analysis to obtain uniform stress distribution in the BP layer. The piezoresistive response was recorded in real time using a digital multimeter (Fluke 289) with a data logging feature. The gauge factor of the SGFRP was calculated from the relation

$$GF = \left(\frac{R - R_0}{R_0} \right) \left(\frac{1}{\varepsilon} \right) \quad (1)$$

where R is the electrical resistance at strained state, R_0 is the original resistance and ε is the longitudinal strain increment.

2.4. Fatigue crack length quantification

The fatigue crack propagation in single edge notch SGFRP specimens (shown in Fig. 4) was investigated next. The specimens were subjected to displacement controlled tension-tension fatigue at a frequency of 5 Hz with strain range of 0.002–0.0065, and the load ratio was approximately 0.2. A measurement model was developed to correlate the fatigue crack length at any instant to the electrical resistance of the SGFRP specimen along the gauge length and *in-situ* resistance readings were recorded during the fatigue tests. Since the loading was uniaxial and pure mode-I, the crack growth was approximately perpendicular to the loading axis. As the crack length increases, a reduction in the effective conducting width of the SGFRP specimen is observed. Based on this, a simple measurement model is derived from the direct current (DC) resistivity equation, accommodating for the reduction in conducting width of the specimen due to increase in crack length, and is given

as

$$R = \frac{\rho L}{t(w - a)} \quad (2)$$

In Equation (2), a is the crack length and R is the measured electrical resistance of the specimen, L is the length of embedded BP (measured between the electrodes), w is the initial average width of BP in the region between electrodes, t is the thickness of the embedded BP and ρ is the electrical resistivity of SGFRP specimen. Fig. 2 shows the SGFRP specimen along with the schematic of the measurement model.

3. Prognosis model development

3.1. Mathematical formulation

The crack propagation behavior in composites under cyclic loads is a highly stochastic and complex process governed by a variety of damage mechanisms that include matrix cracking, fiber breakage

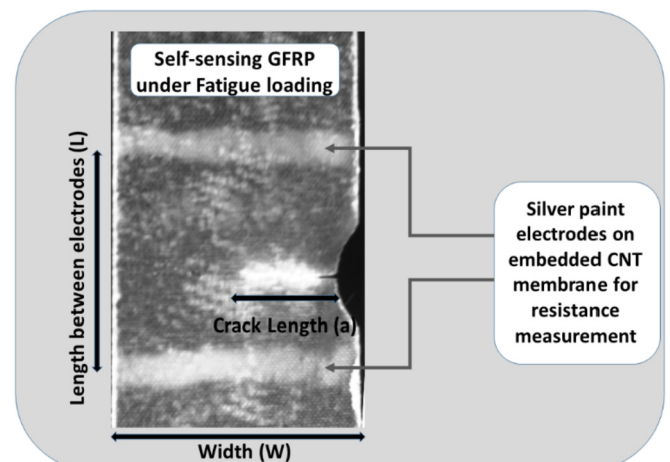


Fig. 2. Schematic of the measurement model for fatigue damage quantification.

and matrix/fiber debonding. Therefore, it is necessary to develop a robust prognosis model to accurately predict the crack propagation under fatigue loading. The hybrid prognosis model developed by Neerukatti et al. is modified to predict the crack propagation by incorporating a cross-validation scheme to improve accuracy [30]. In the model proposed by Neerukatti et al., the crack growth rate at any instant of time is expressed as,

$$\log \frac{da}{dN} = C_1(a_{N-1}, M_p, P_{N,N+1}, N) + C_2(a_{N-1}, M_p, P_{N,N+1}, N) \log(\Delta K) \quad (3)$$

where, M_p is a material parameter and P is the load, ΔK is the stress intensity factor (SIF) range, N is the number of cycles and the coefficients C_1 and C_2 are updated iteratively as more data is obtained. In the original model, the relationship between crack growth rate and SIF was assumed to be linear with varying coefficients. However, since the crack growth in the SGFRP composites exhibited significant crack retardation, the assumption of a linear relationship is not valid. In fact, second and higher order polynomials cannot capture the crack retardation phenomenon due to its highly non linear behavior [34]. Therefore, Gaussian process (GP), which is a machine learning approach, has been used to model the highly nonlinear relationship in this study [35,36]. The primary advantages of using Gaussian process are (i) capability to model arbitrary nonlinear relationships (ii) adaptability with data (iii) making probabilistic predictions. The crack growth rate is assumed to be a random variable which follows a Gaussian distribution [37–39]. GP makes predictions by inferring the underlying nonlinear relationship between input and output spaces. Once the algorithm is trained with the input and output parameters, it can predict the output for a new set of input parameters.

Since the primary driving force for the crack growth is SIF, it is necessary to evaluate the SIF for all possible combinations of crack length and load conditions. Analytical equations cannot be generalized to composite structures whose properties vary with the ply layout [36]. Therefore, the SIF was calculated for different crack tip locations by performing quasi-static finite element analysis (Section 4.4). GP was then used to create a high-dimensional mapping for the SIF as a function of the crack length and applied load as,

$$f(\mathbf{K} | \mathbf{T}_{SIF}, \Phi(\mathbf{x}_i, \mathbf{x}_j), \theta) = \frac{1}{Z} \exp\left(-\frac{(\mathbf{K} - \mu_{\mathbf{K}})^2}{2\sigma_{\mathbf{K}}^2}\right)_{i,j=1,\dots,N_r} \quad (4a)$$

where \mathbf{K} is the vector of SIF evaluated at each point on the test grid, Φ is the kernel matrix, N_r is the number of rows in the grid, $\mathbf{T}_{SIF} = \{\mathbf{x}_i, \mathbf{K}_i\}$; $i = 1, 2, \dots, N_r$ is the training matrix consisting of the crack length, load and SIF obtained from the finite element simulations, Z is a normalizing constant and θ is the vector of hyper-parameters (HPs). The mean and variance of the distribution are obtained as,

$$\mu_{\mathbf{K}} = \varphi_{test}^T \Phi_{train}^{-1}(\mathbf{K})_{train} \sigma_{\mathbf{K}}^2 = \phi - \varphi_{test}^T \Phi_{train}^{-1} \varphi_{test} \quad (4b)$$

where the subscripts *train* and *test* represent the training and test data, respectively. The training data is obtained from the finite element simulations, and the test data are the points on the grid at which the SIF is not known, and ϕ , Φ , φ are the partitioned components of the kernel matrix given by,

$$\begin{aligned} \phi &= k(\mathbf{X}_{test}, \mathbf{X}_{test}) ; \quad \varphi_i = k(\mathbf{X}_{test}, \mathbf{X}_i)_{i=train} ; \quad \Phi_{ij} \\ &= k(\mathbf{X}_i, \mathbf{X}_j)_{i,j=train} \end{aligned} \quad (4c)$$

and k is the kernel function. In this study, squared exponential kernel function (Equation (4d)) has been used as it is capable of modeling complex nonlinear and smooth surfaces.

$$k(\mathbf{x}_i, \mathbf{x}_j) = \theta_1^2 \exp\left(-\frac{(\mathbf{x}_i - \mathbf{x}_j)^2}{\theta_2^2}\right) \quad (4d)$$

The accuracy of prediction depends on the kernel function which depends on the HPs. The optimal HPs are determined by minimizing the negative log marginal likelihood (L) given by,

$$L = -\frac{1}{2} \log \det \Phi_{test} - \frac{1}{2} (\mathbf{K})_{train}^T \Phi_{train}^{-1} (\mathbf{K})_{train} - \frac{N_{train}}{2} \log 2\pi \quad (5)$$

and N_{train} denotes the number of input-output pairs. Once the mapping is created using the above procedure, the value of SIF can be computed for any given point in the grid corresponding to the experimentally obtained crack length and load. The crack growth rate at a given instant of time can be written as:

$$\begin{aligned} f\left(\left(\frac{da}{dN}\right)_N | \mathbf{D}, \mathbf{K}_{N-\Delta N}(\mathbf{x}_i, \mathbf{x}_j), \mathbf{x}_N, \theta\right) \\ = \frac{1}{Z} \exp\left(-\frac{\left(\left(\frac{da}{dN}\right)_N - \mu_{\left(\frac{da}{dN}\right)_N}\right)^2}{2\sigma^2}\right), \end{aligned} \quad (6)$$

where D is the training set consisting of crack length and SIF values (obtained using Equations (4)–(6)).

3.2. Integration of prognosis with resistance based crack data

The resistance based measurement model is now coupled with the fully probabilistic prognosis model in a sequential Bayesian framework to iteratively predict the crack length under fatigue loading. Particle filtering is used to sequentially track the crack length as a function of cycles by combining the likelihood of the measurement model with the posterior obtained from the prognosis model [40,41]. In this methodology, the distribution of the crack length at any given instance is predicted using a prognosis model, and the distribution is then updated using the measurement values in a sequential Bayesian framework. The distribution of the predicted crack length at $N+\Delta N$ cycles, using the prognosis model, can be expressed as follows.

$$p(a_{N+\Delta N}) = p(a_N) + \frac{1}{Z} \exp\left[-\frac{\left(\left(\frac{da}{dN}\right)_N - \mu_{\left(\frac{da}{dN}\right)_N}\right)^2}{2\sigma^2}\right] * \Delta N \quad (7)$$

Together, Equations (4)–(7) define the Markovian state dynamics model for tracking the crack length with particle filter:

$$a_{N+\Delta N} | a_N \sim p(a_{N+\Delta N} | a_N) \quad (8)$$

The measurement model relating the resistance change of the BP to the crack length is given by:

$$a_{N+\Delta N} | R_{N+\Delta N} \sim p(a_{N+\Delta N} | R_{N+\Delta N}) \quad (9)$$

Given the probabilistic state dynamics model and the measurement model, and the resistance values obtained from BP sensing, the crack length can be optimally estimated in a sequential

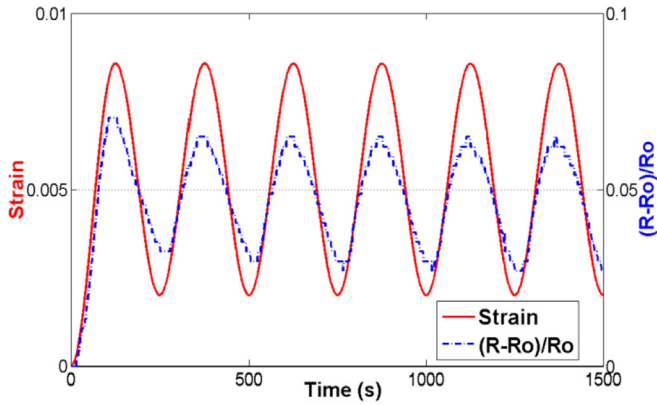


Fig. 3. Piezoresistive response of SGFRP under cyclic loading.

Bayesian framework using particle filter. The posterior distribution of the crack length is iteratively computed as,

$$p(a_N|R_{1:N}) \propto p(R_N|a_N) \int p(a_N|a_{N-\Delta N})p(a_{N-\Delta N}|R_{1:N-\Delta N})d(a_{N-\Delta N}) \quad (10)$$

where $p(\cdot)$ is the conditional probability distribution. The posterior probability distribution is approximated using particles and weights as

$$p(a_N|R_N) = \sum_{k=1}^{\Omega} w_N^{(k)} \delta(a_N - a_N), \quad (11)$$

where Ω is the number of particles and $\delta(\cdot)$ is the Dirac Delta function. Bootstrap particle filtering scheme is employed in which the particles are sampled and updated using the measurement likelihood at each time step [42]. To avoid degeneracy of the weights, resampling is performed at each time step and the weights are normalized such that they sum to one. The crack length is then computed as the expected value of the posterior as,

$$\left(\widehat{d}_s\right)_t = E\left[\left(d_s\right)_t \mid \left(d_s\right)_{t,measured}\right] \approx \sum_{k=1}^M w_t^{(k)} \left(d_s\right)_t^{(k)}. \quad (12)$$

4. Results and discussion

In this section, first the real-time strain sensing results obtained using piezoresistive readings are discussed. Following the strain sensing results, the fatigue crack propagation behavior of SGFRPs and baseline-GFRPs is presented. Finally, the results for *in-situ* fatigue crack length quantification using the measurement model are provided and the crack growth predictions obtained from the prognosis approach are discussed in detail.

Table 1 Sensitivity/Gauge factor during different loading cycles, when SGFRP subjected to cyclic loading.

| Cycle | GF-ascending | GF-descending |
|-------|--------------|---------------|
| 1 | 9.34 | 5.08 |
| 2 | 5.76 | 4.01 |
| 3 | 5.81 | 4.34 |
| 4 | 5.50 | 4.21 |
| 5 | 5.52 | 4.17 |
| 6 | 5.49 | 4.10 |

Table 2 Single-edge notched baseline-GFRPs and SGFRPs tested under fatigue loading.

| Specimen ID | Fatigue life (cycles) | Average Crack growth rate (mm/cycle) |
|-----------------|-----------------------|--------------------------------------|
| SGFRP 1 | 28,620 | 5.58×10^{-4} |
| SGFRP 2 | 16,780 | 4.83×10^{-4} |
| SGFRP 3 | 19,560 | 5.97×10^{-4} |
| SGFRP 4 | 16,200 | 4.98×10^{-4} |
| SGFRP 5 | 18,345 | 5.56×10^{-4} |
| SGFRP 6 | 23,655 | 5.28×10^{-4} |
| Baseline-GFRP 1 | 13,840 | 1.02×10^{-3} |
| Baseline-GFRP 2 | 9050 | 1.61×10^{-3} |
| Baseline-GFRP 3 | 11,240 | 1.42×10^{-3} |
| Baseline-GFRP 4 | 8425 | 1.98×10^{-3} |
| Baseline-GFRP 5 | 8890 | 1.45×10^{-3} |
| Baseline-GFRP 6 | 10,460 | 1.67×10^{-3} |

4.1. Strain sensing

The SGFRP specimens showed stable and repeatable piezoresistive response under cyclic loading. The resistance change with cyclic strain for a representative specimen is shown in Fig. 3. The piezoresistive response shows negligible phase lag with strain, indicating strong adhesion and minimal slippage at the glass fiber/BP interface. The gauge factor was found to be higher for the first loading cycle (9.34 for ascending and 5.08 for descending) as compared to the subsequent loading cycles, retaining a stable sensitivity over the next five cycles with an average value of 5.62 for ascending and 4.17 for descending segments of the cycles. The sensitivity values for each cycle for the representative specimen are presented in Table 1. Higher sensitivity in the first cycle can be attributed to additional interactions at the BP/glass-fiber interface. The effect of this extra interaction diminishes after the first cycle as polymer relaxation takes place, and the sensitivity reduces to a stable value. The sensitivity values are significantly higher than those obtained using commercially available conventional strain gauges as well several CNT based composite sensors reported in literature [27,43–45]. The higher sensitivity is a promising feature, allowing very low strains to be detected with a measurable resistance change. Delamination was observed at the BP/glass-fiber interface of the composite after 80,000 cycles indicating end of functional life of the embedded sensor. The fatigue tests were terminated after 200,000 cycles and complete failure of the specimen was not observed. However, consistent load drop after 100,000 cycles could be an indicative of cyclic softening in the polymer matrix.

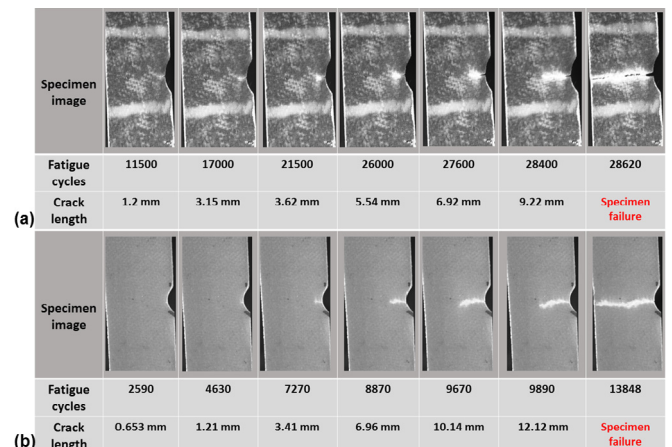


Fig. 4. Fatigue crack propagation in: (a) SGFRP specimen; (b) baseline-GFRP specimen.

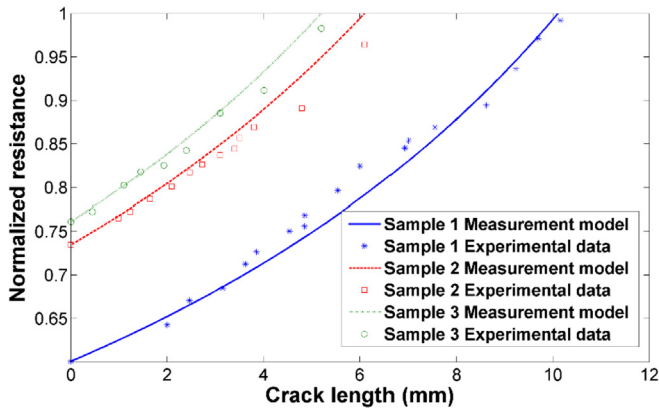


Fig. 5. Normalized resistance trends with fatigue crack extension.

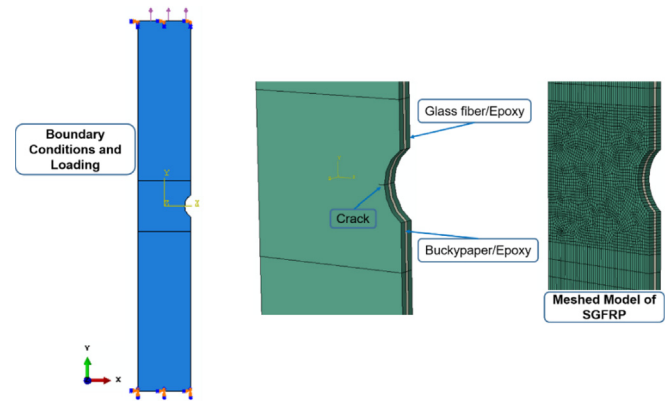


Fig. 7. Finite element model of the single edge notch SGFRP specimen.

4.2. Fatigue crack propagation

Single-edge notched specimens of baseline-GFRP and SGFRP tested under fatigue loading are summarized in Table 2. Series of images obtained for the SGFRP specimens at progressive stages of the fatigue test are presented in Fig. 4a, where the trend in crack propagation is representative of six specimens tested under the same fatigue loading. The average crack growth rate from six specimens was found to be 5.36×10^{-4} mm/cycle over the stable crack propagation regime (between crack initiation and fast fracture regime). In comparison, the average crack growth rate in baseline-GFRP specimens after crack initiation was found to be 1.53×10^{-3} mm/cycle, which is significantly higher than SGFRPs. The significant reduction in the fatigue crack growth rate due to the introduction of BP in the interlaminar region of the GFRP laminates can be explained as follows. The presence of the randomly oriented and densely entangled microstructure of the embedded BP results in a highly torturous crack path leading to retardation in the fatigue crack growth rate and even crack arrest at various instances during crack propagation. As shown in Fig. 4a, the crack path in SGFRPs was highly torturous and crack tip blunting is observed at various stages of the fatigue test. From Fig. 4a it can be observed that during crack propagation from 15,000 to 21,500 fatigue cycles, the crack tip becomes blunt without noticeable increase in crack length. Fig. 4b shows fatigue crack propagation trend in one of the baseline-GFRP specimens where a relatively sharp and defined crack tip can be observed and the trend is representative of six baseline-GFRP specimens tested under the same fatigue loading.

This observation points to an additional crack deceleration type attribute of the SGFRP.

4.3. Damage quantification

The experimentally obtained values of electrical resistance at different crack lengths, normalized with respect to the maximum resistance from the measurement model, are presented in Fig. 5 as a function of instantaneous crack lengths for three specimens. The resistance trends as a function of crack length were found to be in close agreement with the measurement model presented in section 2.4 (Eq. (2)). The resistance readings were successfully obtained during the fatigue crack growth prior to the occurrence of fast fracture. Fig. 6 shows good agreement between the crack lengths quantified in SGFRPs using the *in-situ* electrical resistance measurements and those obtained using the high-resolution camera.

4.4. Damage prognosis

As mentioned earlier, the prognosis model fuses analysis results with machine learning models. The primary physics based parameter for the fatigue crack propagation is the SIF, for which closed form solutions are not available, especially for composites. Therefore, finite element analysis (FEA) was used to evaluate the SIF [46]. Values of SIF were obtained by performing 50 FEA simulations

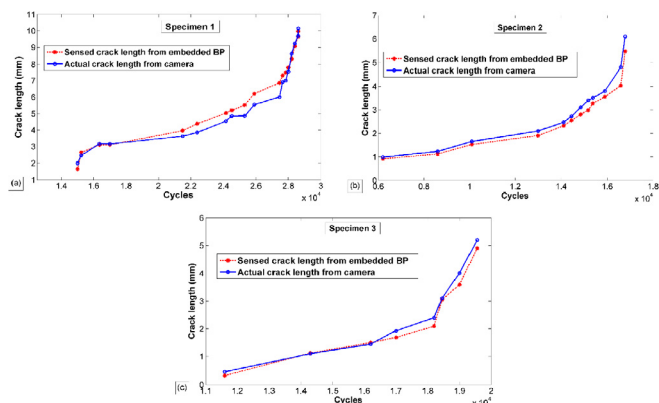


Fig. 6. Actual crack lengths and sensed crack lengths as a function of fatigue cycles for 3 specimens.

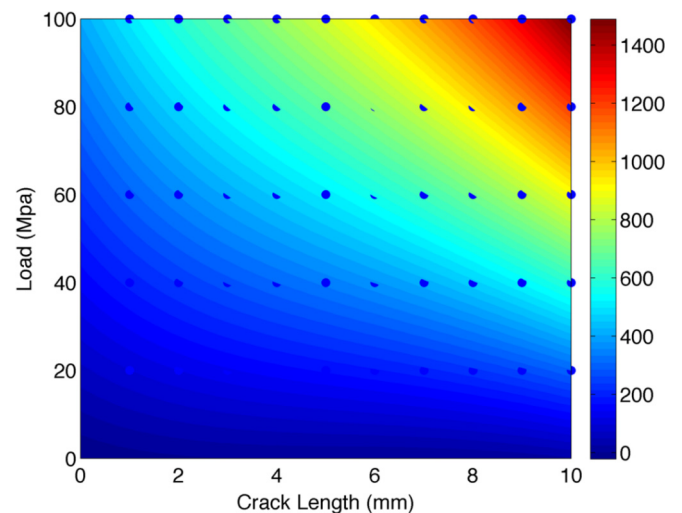


Fig. 8. SIF mapping as a function of crack length and load.

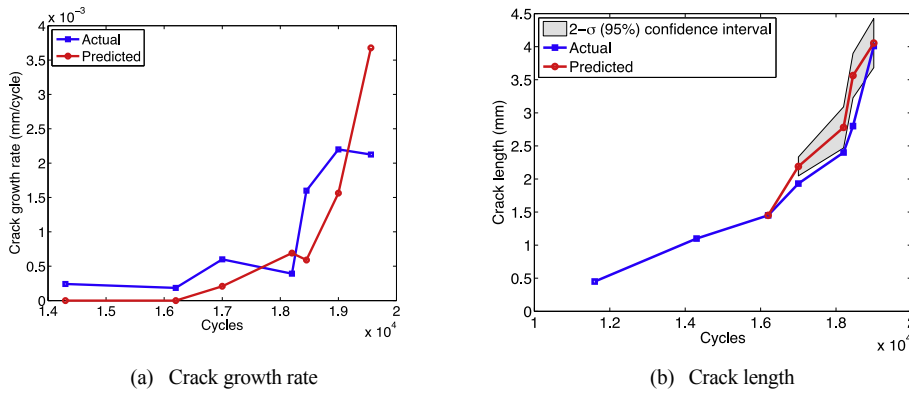


Fig. 9. Crack length predictions for sample 3.

on the single edge notch SGFRP with different combinations of loads (20–100 MPa) and crack lengths (1–10 mm). The FEA mesh of the single edge notch SGFRP specimen was spatially discretized in the commercially available FE package Abaqus CAE using 15,738 linear hexahedral elements (Type C3D8R) and is shown in Fig. 7. Perfect bonding was assumed between the BP and glass fiber layers. Displacement boundary conditions were applied at the bottom nodes to restrict motion in the x, y and z directions and on the top nodes to restrict motion in the x and z directions, as shown in Fig. 7. Surface traction was applied at the top surface to simulate the applied tensile loading. For the FEA simulations, material properties used for glass fiber/epoxy layers and BP/epoxy layer were experimentally obtained from quasistatic tensile tests.

In order to obtain the SIF value for any given load and crack length obtained during the experiment, a mapping was created using GP using Equations (3)–(5) and is shown in Fig. 8. A total of 50 simulations were performed with load varying from 0 to 100 MPa with increments of 20 MPa and the crack length varying from 0 to 10 mm with increments of 2 mm. The GP model was used to create a mapping (fit a surface) to these points. From this mapping, the SIF can be evaluated for any given pair of load and crack length values. A coefficient of determination of 0.9914 was obtained for the mapping which indicates a highly accurate fit. The contour shows that the relationship between the load, crack length and SIF is highly nonlinear and therefore, simple regression models cannot be used to model the relationship.

The crack length was predicted using the integrated prognosis model described in Section 3. Fig. 9 shows the predictions of crack growth rate and crack length as a function of cycles starting at the 3rd data point (measurement) for sample 3. The results indicate

that the crack length is predicted accurately within the 95% confidence intervals.

Next, the algorithm was used to make predictions for sample 1. Fig. 10 shows the crack growth rate and crack length as a function of the number of cycles. The crack growth rate plot indicates a significant amount of crack retardation and acceleration due to the presence of the BP. Fig. 10b show that the proposed approach is capable of capturing these effects and predicting the crack length with a high level of accuracy.

5. Conclusions

BPs fabricated using MWCNTs were embedded in GFRPs to successfully induce self-sensing capabilities and improved fatigue resistance in GFRP laminates. The results for SGFRPs tested under cyclic tensile loading showed high sensitivity to strain over a significant strain range. An *in-situ* measurement model was developed to quantify the damage evolution with change in electrical resistance; close correlation was observed with experimentally obtained fatigue crack data. A comparison of fatigue crack propagation trends conducted on the test specimens at various stages of fatigue showed a significantly lower crack growth rate for the specimens with embedded BP. These results point to the multifunctional nature of the BP embedded composites.

An integrated approach for predicting real-time crack propagation was developed by combining the BP based measurement model with a machine learning based prognosis model in a sequential Bayesian framework. SIF was used as the physics based parameter for crack growth. The results indicate that the proposed methodology is capable of accurately predicting the crack length in

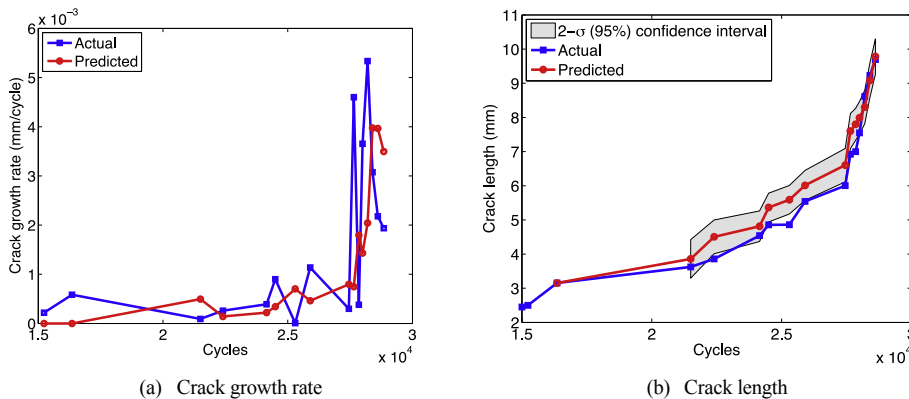


Fig. 10. Crack length predictions for sample 1.

real-time while accommodating for crack retardation.

Acknowledgments

The authors gratefully acknowledge the support of this research by the Office of Naval Research (ONR; Grant N00014-17-1-2037) and program manager Mr. William Nickerson.

References

- [1] D. Balageas, C. Fritzen, A. Güemes, *Structural Health Monitoring*, John Wiley & Sons, 2010.
- [2] V. Giurgiutiu, A. Zagrai, J. Jing Bao, Piezoelectric wafer embedded active sensors for aging aircraft structural health monitoring, *Struct. Health Monit.* 1 (2002) 41–61.
- [3] N. Alexopoulos, C. Bartholome, P. Poulin, Z. Marioli-Riga, Structural health monitoring of glass fiber reinforced composites using embedded carbon nanotube (CNT) fibers, *Composites Sci. Technol.* 70 (2010) 260–271.
- [4] I. Kang, M.J. Schulz, J.H. Kim, V. Shanov, D. Shi, A carbon nanotube strain sensor for structural health monitoring, *Smart Mater. Struct.* 15 (2006) 737.
- [5] P. Dharap, Z. Li, S. Nagarajah, E. Barrera, Nanotube film based on single-wall carbon nanotubes for strain sensing, *Nanotechnology* 15 (2004) 379.
- [6] L. Böger, M.H. Wichmann, L.O. Meyer, K. Schulte, Load and health monitoring in glass fibre reinforced composites with an electrically conductive nanocomposite epoxy matrix, *Composites Sci. Technol.* 68 (2008) 1886–1894.
- [7] X. Yu, E. Kwon, A carbon nanotube/cement composite with piezoresistive properties, *Smart Mater. Struct.* 18 (2009), 055010.
- [8] A. Rai, N. Subramanian, A. Chattopadhyay, Investigation of piezo-resistivity in CNT nano-composites under damage, *SPIE smart structures and materials nondestructive evaluation and health monitoring*, Anon. Int. Soc. Optics Photonics (2016) 980017.
- [9] J.N. Coleman, U. Khan, W.J. Blau, Y.K. Gun'ko, Small but strong: a review of the mechanical properties of carbon nanotube–polymer composites, *Carbon* 44 (2006) 1624–1652.
- [10] A. Allaoui, S. Bai, H. Cheng, J. Bai, Mechanical and electrical properties of a MWNT/epoxy composite, *Composites Sci. Technol.* 62 (2002) 1993–1998.
- [11] F. Gojny, M. Wichmann, U. Köpke, B. Fiedler, K. Schulte, Carbon nanotube-reinforced epoxy-composites: enhanced stiffness and fracture toughness at low nanotube content, *Composites Sci. Technol.* 64 (2004) 2363–2371.
- [12] F.H. Gojny, M.H. Wichmann, B. Fiedler, K. Schulte, Influence of different carbon nanotubes on the mechanical properties of epoxy matrix composites—a comparative study, *Composites Sci. Technol.* 65 (2005) 2300–2313.
- [13] F.H. Gojny, M.H. Wichmann, B. Fiedler, W. Bauhofer, K. Schulte, Influence of nano-modification on the mechanical and electrical properties of conventional fibre-reinforced composites, *Compos. Appl. Sci. Manuf.* 36 (2005) 1525–1535.
- [14] O. Meincke, D. Kaempfer, H. Weickmann, C. Friedrich, M. Vathauer, H. Warth, Mechanical properties and electrical conductivity of carbon-nanotube filled polyamide-6 and its blends with acrylonitrile/butadiene/styrene, *Polymer* 45 (2004) 739–748.
- [15] Z. Spitalsky, D. Tasis, K. Papagelis, C. Galiotis, Carbon nanotube–polymer composites: chemistry, processing, mechanical and electrical properties, *Prog. Polym. Sci.* 35 (2010) 357–401.
- [16] N. Subramanian, A. Rai, S. Datta, B. Koo, A. Chattopadhyay, A multiscale model coupling molecular dynamics simulations and micromechanics to study the behavior of CNT-enhanced, *Nanocomposites* (2015) 0390.
- [17] S. Datta, M.Y. Fard, A. Chattopadhyay, Fatigue Crack Growth Behavior of Hybrid Glass Fiber Laminates with Embedded Functionalized Carbon Nanotube Membranes, 2016. V009T12A067–V009T12A067.
- [18] M.Y. Fard, J.M. Woodward, S. Datta, B. Raji, A. Chattopadhyay, Characterization of Interlaminar Fracture Properties of Advanced Polymer Matrix Composites Interleaved with Bucky paper, 2016. V009T12A083–V009T12A083.
- [19] A. Rai, N. Subramanian, B. Koo, A. Chattopadhyay, Multiscale damage analysis of carbon nanotube nanocomposite using a continuum damage mechanics approach, *J. Composite Mater.* 51 (2017) 847–858.
- [20] K.J. Kim, W. Yu, J.S. Lee, L. Gao, E.T. Thostenson, T. Chou, et al., Damage characterization of 3D braided composites using carbon nanotube-based in situ sensing, *Compos. Appl. Sci. Manuf.* 41 (2010) 1531–1537.
- [21] L. Vertuccio, V. Vittoria, L. Guadagno, F. De Santis, Strain and damage monitoring in carbon-nanotube-based composite under cyclic strain, *Compos. Appl. Sci. Manuf.* 71 (2015) 9–16.
- [22] P. Slobodian, P. Riha, A. Lengalová, P. Svoboda, P. Saha, Multi-wall carbon nanotube networks as potential resistive gas sensors for organic vapor detection, *Carbon* 49 (2011) 2499–2507.
- [23] C. Zheng, W. Qian, Y. Yu, F. Wei, Ionic liquid coated single-walled carbon nanotube buckypaper as supercapacitor electrode, *Particuology* 11 (2013) 409–414.
- [24] X. Fu, C. Zhang, T. Liu, R. Liang, B. Wang, Carbon nanotube buckypaper to improve fire retardancy of high-temperature/high-performance polymer composites, *Nanotechnology* 21 (2010), 235701.
- [25] J.G. Park, J. Louis, Q. Cheng, J. Bao, J. Smithyman, R. Liang, et al., Electromagnetic interference shielding properties of carbon nanotube buckypaper composites, *Nanotechnology* 20 (2009), 415702.
- [26] H. Chu, Z. Zhang, Y. Liu, J. Leng, Self-heating fiber reinforced polymer composite using meso/macropore carbon nanotube paper and its application in deicing, *Carbon* 66 (2014) 154–163.
- [27] M. Rein, O. Breuer, H. Wagner, Sensors and sensitivity: carbon nanotube buckypaper films as strain sensing devices, *Composites Sci. Technol.* 71 (2011) 373–381.
- [28] Z. Zhang, H. Wei, Y. Liu, J. Leng, Self-sensing properties of smart composite based on embedded buckypaper layer, *Struct. Health Monit.* 14 (2015) 127–136.
- [29] A. Rai, S. Datta, A. Chattopadhyay, C. Lopez, Reinforcement of Composite Joint Interface Using Nanomaterials, 2017. V009T12A002–V009T12A002.
- [30] R.K. Neerukatti, K.C. Liu, N. Kovvali, A. Chattopadhyay, Fatigue life prediction using hybrid prognosis for structural health monitoring, *J. Aero. Inf. Syst.* 11 (2014) 211–232.
- [31] R.K. Neerukatti, M.Y. Fard, A. Chattopadhyay, Gaussian process-based particle-filtering approach for real-time damage prediction with application, *J. Aerospace Eng.* 30 (2016), 04016080.
- [32] A. Doucet, N. De Freitas, N. Gordon, *An Introduction to Sequential Monte Carlo Methods*, Sequential Monte Carlo Methods in Practice, Springer, 2001, pp. 3–14.
- [33] S. Datta, M.Y. Fard, A. Chattopadhyay, High-speed surfactant-free fabrication of large carbon nanotube membranes for multifunctional composites, *J. Aerospace Eng.* 29 (2015), 04015060.
- [34] Z. Domazet, Comparison of fatigue crack retardation methods, *Eng. Fail. Anal.* 3 (1996) 137–147.
- [35] C.E. Rasmussen, *Gaussian Processes for Machine Learning*, 2006.
- [36] W. Zhang, R. Picu, N. Koratkar, Suppression of fatigue crack growth in carbon nanotube composites, *Appl. Phys. Lett.* 91 (2007), 193109.
- [37] S. Mohanty, S. Das, A. Chattopadhyay, P. Peralta, Gaussian process time series model for life prognosis of metallic structures, *J. Intell. Mater. Syst. Struct.* 20 (2009) 887–896.
- [38] S. Mohanty, A. Chattopadhyay, P. Peralta, S. Das, Bayesian statistic based multivariate Gaussian process approach for offline/online fatigue crack growth prediction, *Exp. Mech.* 51 (2011) 833–843.
- [39] S. Mohanty, A. Chattopadhyay, P. Peralta, On-line Life Prediction of a Structural Hotspot, 2008, pp. 297–304.
- [40] A. Doucet, N. De Freitas, N. Gordon, *An Introduction to Sequential Monte Carlo Methods*, Sequential Monte Carlo Methods in Practice, Springer, 2001, pp. 3–14.
- [41] R.K. Neerukatti, K. Hensberry, N. Kovvali, A. Chattopadhyay, A novel probabilistic approach for damage localization and prognosis including temperature compensation, *J. Intell. Mater. Syst. Struct.* 27 (2016) 592–607.
- [42] N.J. Gordon, D.J. Salmond, A.F. Smith, *Novel Approach to Nonlinear/non-Gaussian Bayesian State Estimation*, vol. 140, 1993, pp. 107–113.
- [43] T. Yamada, Y. Hayamizu, Y. Yamamoto, Y. Yomogida, A. Izadi-Najafabadi, D.N. Futaba, et al., A stretchable carbon nanotube strain sensor for human-motion detection, *Nat. Nanotechnol.* 6 (2011) 296–301.
- [44] X. Li, C. Levy, L. Elaadil, Multiwalled carbon nanotube film for strain sensing, *Nanotechnology* 19 (2008), 045501.
- [45] A. Ferreira, J. Rocha, A. Ansón-Casaos, M. Martínez, F. Vaz, S. Lanceros-Mendez, Electromechanical performance of poly (vinylidene fluoride)/carbon nanotube composites for strain sensor applications, *Sensor Actuator Phys.* 178 (2012) 10–16.
- [46] J. Rice, D.M. Tracey, *Computational Fracture Mechanics*, Numerical and Computer Methods in Structural Mechanics, Elsevier, 1973, pp. 585–623.